



ELSEVIER

Available online at www.sciencedirect.com

SCIENCE @ DIRECT®

Journal of Magnetism and Magnetic Materials 288 (2005) 354–365

Journal of
magnetism
and
magnetic
materials

www.elsevier.com/locate/jmmm

Magnetic order in γ -Fe₂O₃ nanoparticles: a XMCD study

S. Brice-Profeta^{a,*}, M.-A. Arrio^a, E. Tronc^b, N. Menguy^a, I. Letard^a,
C. Cartier dit Moulin^{c,d}, M. Noguès^e, C. Chanéac^b,
J.-P. Jolivet^b, Ph. Saintavitt^{a,d}

^aLaboratoire de minéralogie-cristallographie de Paris, UMR 7590, CNRS/IPGP/UPMC/UDD, Case 115, 4 place Jussieu, F-75252 Paris Cedex 05, France

^bLCMC, UMR 7514 CNRS/UPMC, Case 174, 4 place Jussieu, F-75252 Paris Cedex 05, France

^cLCI2M, UMR 7071 CNRS/UPMC, Case 42, 4 place Jussieu, F-75252 Paris Cedex 05, France

^dLURE, UMR 130 CNRS/CEA/MENRT, Bât 209D, BP 34, F-91898 Orsay, France

^eLMOV, UMR 8634 CNRS/UVSQ, 45 av. des États-Unis, F-78035 Versailles, France

Received 1 April 2004; received in revised form 2 September 2004

Available online 20 October 2004

Abstract

Spin-canting in spinel nanoparticles of maghemite has multiple origins, among which surface effects, finite-size effects or chemical disorder effects. XMCD at the Fe L_{2,3} edges allows to separate the contributions of the magnetic moments of Fe³⁺ ions in tetrahedral and octahedral sites of γ -Fe₂O₃. We investigate three powders of γ -Fe₂O₃ synthesized via aqueous precipitation: particles of average diameter 2.7, 8 nm and particles of average diameter 8 nm coated with phosphoric acid. The relative contributions of the spins of the Fe_{Td}³⁺ and the Fe_{Oh}³⁺ ions are observed, varying the external magnetic field. Under high magnetic fields, a reduction of the magnetic contribution of the Fe_{Oh}³⁺ ions occurs for 8 nm phosphate-coated particles by comparison with the uncoated ones. A similar reduction appears at lower magnetic fields for the small 2.7 nm particles.

© 2004 Elsevier B.V. All rights reserved.

Keywords: Maghemite nanoparticles; γ -Fe₂O₃; XMCD; Spin-canting; Iron L_{2,3} edges

1. Introduction

Magnetic properties of nanoparticles of ferro- and ferrimagnetic materials with typical sizes

ranging from 0.5 to 10 nm have been investigated for many years (for a review, see Ref. [1] and references therein). Knowledge of the magnetic behavior of fine grains is crucial as regard to their numerous occurrences in technological applications. For instance, iron oxide nanoparticles are components of ferrofluids, biomedical materials, catalysts or magnetic recording media [2].

*Corresponding author. Tel.: +33 144 279 832; fax: +33 144 273 785.

E-mail address: Sandrine.Brice@lmcp.jussieu.fr
(S. Brice-Profeta).

0304-8853/\$ - see front matter © 2004 Elsevier B.V. All rights reserved.

doi:10.1016/j.jmmm.2004.09.120

Magnetic nanoparticles are also research tools in areas of physics, geology, biology and medicine.

Magnetic properties of fine particles strongly depend on surface effects, finite-size effects and interparticles interactions [1,3]. Magnetic properties of nanoparticles differ from those of the bulk materials. Below a critical diameter of typically 10–100 nm, nanoparticles are single magnetic domains, and exhibit a superparamagnetic behavior [4]. Oxide nanocrystallites often have larger coercivities than bulk materials, due to a reinforcement of the surface magnetic anisotropy. A reduction of the saturating magnetization generally occurs in ferro- or ferrimagnets such as γ -Fe₂O₃ (maghemite), NiFe₂O₄ or CoFe₂O₄ [3]. On the contrary, nanoparticles of antiferromagnetic materials may have a non zero magnetic moment. That is the case of hematite (α -Fe₂O₃) nanoparticles, due to a canted antiferromagnetism [5]. The origin of the magnetization reduction in spinel nanoparticles is still unclear. It is generally accepted that surface spins are canted, due to competing exchange interactions in an incomplete coordination shell for surface ions [6]. In the case of γ -Fe₂O₃, however, identical degrees of canting has been found using in-field Mössbauer spectroscopy in γ -Fe₂O₃ nanoparticles, with either ⁵⁷Fe-enriched surface or without it [7]. This tends to prove that the canting could also be a finite-size effect, and may affect the volume of the particles. Morales et al. investigated a series of γ -Fe₂O₃ nanoparticles of \sim 100 nm with various degrees of vacancies ordering and of chemical disorder ascribed to the presence of hydroxide groups in the structure [8]. Their results show that spin canting can arise from structural disorders in maghemite as well. In general, modifications of the magnetic properties with respect to those of bulk materials are very sensitive to the way the particles are elaborated, that is, to the surface and the local chemical structure of the particles. Spin canting in nanoparticles is probably dramatically dependent on chemical irregularities in the whole particle, and more specifically at the surface. A precise knowledge of the chemical state of the surface should be valuable in understanding the magnetic properties of fine particles.

X-ray magnetic circular dichroism (XMCD) at the L_{2,3} edges of transition elements is now widely used as a local probe for the site symmetry and the magnetic moments of transition-metal ions in ferro- and ferrimagnetic materials. The dichroic signal is the difference between the absorption cross-sections for right- and left-circularly polarized X-ray under an external magnetic field applied along the X-ray propagation vector. This paper reports about the use of X-ray absorption spectroscopy (XAS) and XMCD at the iron L_{2,3} edges on γ -Fe₂O₃ nanoparticles to study the effects of the size of maghemite nanoparticles both on their chemical and magnetic structures.

γ -Fe₂O₃ has a spinel structure that belongs to the space group symmetry Fd $\bar{3}$ m and can be described by the following formula: Fe_A³⁺[Fe_{5/3}³⁺□_{1/3}]_BO₄. A represents a tetrahedral site, B an octahedral site and □ a cationic vacancy on the octahedral sublattice. γ -Fe₂O₃ is the fully oxidized form of magnetite (Fe₃O₄). The nanoparticles of γ -Fe₂O₃ investigated here are synthesized by aqueous precipitation of magnetite, followed by an oxidation to maghemite under acidic conditions. Synthesis details can be found in Ref. [9]. Samples of particles with different average diameters are obtained, depending on the ionic strength of the synthesis medium. They have a mono-modal lognormal size distribution. Due to the elaboration method, there is no ordering of the vacancies. To vary the surface to volume ratio of the particles, powdered samples of small particles (denoted as S), with an average diameter of 2.7 nm, and of medium-sized particles (denoted as M) with an average diameter of 8 nm are studied. In-field Mössbauer spectroscopy and magnetization measurements were carried out to characterize the magnetic properties of those samples. ⁵⁷Fe Mössbauer spectra in an applied magnetic field of 6 T at 10 K show indications of a canted spin structure over a wide range of temperature [9,10]. The spin canting increases as the size of the nanoparticles decreases.

Since the surface state is likely to influence strongly the magnetic properties of γ -Fe₂O₃ nanoparticles, we also work on particles of average diameter 8 nm coated with phosphoric acid (denoted as MP). The binding mode of the ligands at the surface of γ -Fe₂O₃ has been determined,

thanks to IR spectra in a previous work [9]. The phosphate groups are bonded to Fe^{3+} in unidentate and bridging bidentate coordination modes. Such a coating modifies the surface state and alters the magnetic order of the surface layer in comparison with an uncoated surface. Indeed, X-ray diffraction patterns exhibit two diffuse bands, that are likely to be due to ferric phosphate complexes with a distorted symmetry around the metal [9]. In addition, zero-field and in-field Mössbauer spectra points out that MP particles consists of a γ - Fe_2O_3 core surrounded by a magnetically totally disordered phosphated iron shell.

We aim at clarifying the role of the chemical structure of γ - Fe_2O_3 nanoparticles, especially as far as the surface is concerned, in their magnetic properties. To draw a link between the local environment of atoms and the degree of alignment of the spins along the external field at high magnetic field on the three samples of nanoparticles (S, M and MP), XAS and XMCD signals with an external field of 2 T are recorded at the iron $L_{2,3}$ edges at 4.2 K. In the following, the global lack of alignment of either Fe_A^{3+} or Fe_B^{3+} spins on the external field will be designated as “spin canting”. Previous measurements on those samples underline that their static and dynamic magnetic properties are consistent with a core–shell model [10]. At high external magnetic fields (and low temperatures), the magnetization of the surface shell is equal to the core magnetization. At lower external magnetic field, the magnetization due to the surface shell reduces. Hence, XMCD data are also collected on the S, M and MP samples, varying the external magnetic field from 0 to 2 T at 4.2 K. Thanks to the thin probing depth in the soft X-ray range, surface effects should be emphasized in absorption and dichroism at the iron $L_{2,3}$ edges. According to Ref. [11], the probing depth at the $L_{2,3}$ edges of iron is typically of 45 Å in the case of iron oxides.

2. Experimental details and theoretical framework

2.1. HRTEM

High Resolution Transmission Electron Microscopy (HRTEM) experiments have been carried

out on a Jeol 2010F microscope operating at 200 kV, equipped with a high-resolution UHR pole piece and a Gatan energy filter GIF 100. Images are taken using elastically scattered electrons. Maghemite particles are deposited on a carbon film.

2.2. X-ray absorption and XMCD

We recorded the absorption spectra at $L_{2,3}$ edges of iron on three samples of γ - Fe_2O_3 both on the SU23 beamline of the storage ring Super-ACO at LURE (Orsay, France) and on the BACH beamline (Beamline for Advanced diCHroic experiments) at the ELETTRA synchrotron radiation source (Trieste, Italy) [12]. The experimental end-station on the two beamlines was identical. It is a cryostat developed by Kappler and Saintavit [13]. The sample temperature is set, thanks to a pumped ^4He cryostat, reaching temperatures ranging from 1.5 to 300 K. The external magnetic field is generated by a superconducting coil and varies from -7 to 7 T. The magnetic field is perpendicular to the surface of the sample holder, and parallel to the X-rays propagation vector. Powders are deposited on a copper plate to insure good electrical and thermal conductivities. Absorption spectra are collected in the total electron yield (TEY) mode. The photocurrent is measured with a Keithley 617 electrometer.

For circularly polarized X-rays, the absorption cross-sections can be labeled as σ^{ab} . a denotes the helicity of the photons. $a = \downarrow$ when the photons are right-hand polarized and $a = \uparrow$ when the photons are left-hand polarized. b denotes the direction of the magnetic field. $b = \uparrow$ (resp. $b = \downarrow$) when the magnetic field is parallel (resp. antiparallel) to the propagation vector \mathbf{k} . In the electric dipole approximation, reversing the magnetic field is equivalent to changing the helicity of the beam, i.e. $\sigma^{\uparrow\uparrow} = \sigma^{\downarrow\downarrow}$ and $\sigma^{\uparrow\downarrow} = \sigma^{\downarrow\uparrow}$ [14]. A dichroic spectra thus results from the difference of two absorption cross-sections, reversing either the photon helicity or the external magnetic field. By convention, $\sigma_{\text{XMCD}} = \sigma^{\uparrow\downarrow} - \sigma^{\downarrow\uparrow}$ for a 100% circular polarization. The experimental dichroic signal has to be normalized to a 100% polarization rate, by taking into account τ ,

the experimental polarization rate: $\sigma_{\text{XMCD}} = 1/|\tau| (\sigma^{\uparrow\downarrow} - \sigma^{\uparrow\uparrow})$.

On SU23 at Super-Aco, the X-ray beam is produced by an asymmetric wiggler that delivers elliptically polarized light above and below the orbit plane. The focussing of the beam is performed through a set of toroidal and spherical mirrors. The elliptically polarized white beam is monochromatized by a grating of a groove density of 1800 lines/mm. The polarization rate of the photons on the sample is estimated to be $\tau = 42\%$. The instrumental resolving power is $E/\Delta E \sim 3500$. Dichroic signals are obtained by flipping the direction of the magnetic field between two energy scans. On the BACH beamline, the insertion devices are two APPLE-II undulators [12]. We used the first harmonic of the high-energy undulator. The monochromator is a spherical grating of a groove density of 400 lines/mm giving an intensity of 7×10^{11} photons s^{-1} on the sample at the energy of the L_3 edge of iron. The polarization rate is almost 100%. The resolution power is estimated to be 1500. In the data collection procedure, each dichroic signal is derived from four spectra: for each magnetic field, the sign of the phase of the undulator is reversed between two spectra, giving the absorptions $\sigma^{\uparrow\uparrow}$ and $\sigma^{\downarrow\uparrow}$. The field is flipped after the first two spectra, giving the absorptions $\sigma^{\uparrow\downarrow}$ and $\sigma^{\downarrow\downarrow}$. In this case, $\sigma_{\text{XMCD}} = 1/\tau ((\sigma^{\uparrow\downarrow} + \sigma^{\uparrow\uparrow}) - (\sigma^{\downarrow\uparrow} + \sigma^{\downarrow\downarrow}))/2$. The ability to reverse the photons helicity allows to compensate for systematic errors during the measurement process.

2.3. Multiplet theory

In order to extract quantitative informations, the XAS and XMCD spectra at the iron $L_{2,3}$ edges are simulated using ligand field multiplet (LFM) calculations developed by Theo Thole [15]. We expose here briefly the principles of multiplet calculations. More details can be found in Refs. [16–19]. Iron $L_{2,3}$ edges consist mainly of the dipole allowed $2p^63d^5 \rightarrow 2p^53d^6$ transitions, as the dipole allowed $2p^64s^0 \rightarrow 2p^54s^1$ transitions have a negligible contribution to the absorption cross-section. In spherical symmetry, the $2p^63d^5$ ground state and the $2p^53d^6$ excited state energy

levels are split by the interelectronic repulsions and the spin–orbit coupling. The radial integrals for interelectronic repulsions and spin orbit coupling are calculated using Cowan’s atomic Hartree–Fock code [16]. One has to take into account for the initial $2p^63d^5$ configuration, the direct $F^2(3d,3d)$ and $F^4(3d,3d)$ Slater integrals and the 3d shell spin–orbit coupling parameter ζ_{3d} , and the excited $2p^53d^6$ configuration, the direct $F^2(3d,3d)$, $F^4(3d,3d)$, $F^2(2p,3d)$ Slater integrals, the exchange $G^1(2p,3d)$, $G^3(2p,3d)$ Slater integrals, the 2p shell spin–orbit coupling ζ_{2p} and ζ_{3d} . The Slater integrals are reduced using the κ parameter. This reduction accounts for the electronic delocalization occurring through the chemical bonding in the solid. The effect of the crystal field and of the local magnetic field at the absorbing atom is treated using Butler’s group subduction [17]. For octahedral and tetrahedral sites of the spinel structure, the O_3-O_h and the O_3-T_d branchings are used. The crystal field is then described by a single parameter, $10Dq$. The local magnetic field appears in the Zeeman hamiltonian: $\mathcal{H}_{\text{Zee}} = g\mu_B H S_z$. In ferro- and ferrimagnetic oxides, the $g\mu_B H$ parameter may typically range from 5 to 100 meV [20]. The energy and the intensities of the transitions are calculated in the electric dipole approximation. To simulate the experimental XAS spectra and XMCD signals, the transition lines are broadened by a Lorentzian function to account for the core–hole lifetime, and by a Gaussian function to account for the instrumental resolution.

3. Results and discussion

3.1. HRTEM

Determinations of the size of the S, M and MP particles have been carried out previously, using X-ray diffraction and TEM pictures [21]. As spin disorder in powders of $\gamma\text{-Fe}_2\text{O}_3$ nanoparticles is likely to arise from surface atoms, we are interested in characterizing the surface of the particles. HRTEM pictures of the M particles have been taken. Fig. 1 is representative of what has been observed on several tens of particles. From this image, it can be inferred that the nanoparticles are

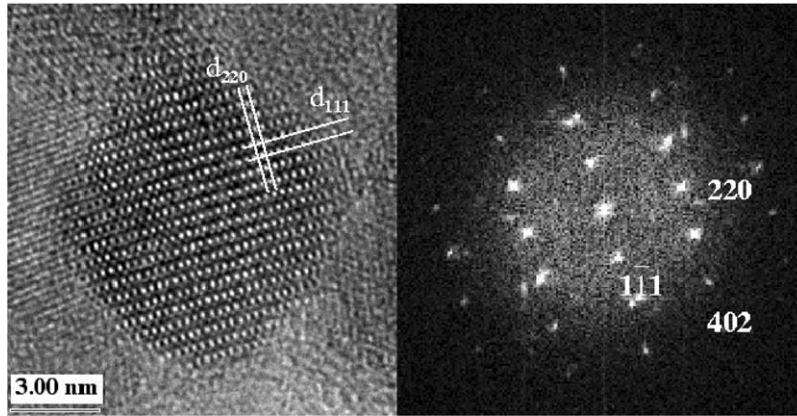


Fig. 1. HRTEM image of the 8 nm γ -Fe₂O₃ nanoparticles (M sample), and the corresponding electronic diffraction pattern.

well-crystallized and exhibit well-defined faceted edges. There is no preferential crystallographic orientation of these faceted edges. One or several preferential orientations could have informed on the type of crystallographic sites at the surface of the particles. Indeed, the tetrahedral to octahedral sites ratio, denoted as A/B, can differ at the surface from the ideal sites ratio of $3/5 = 0.6$ in case of the existence of preferential surface planes. HRTEM images stand in agreement with former XRD results since no shape anisotropy is observed.

3.2. Shape analysis of XAS and XMCD in the multiplet framework

Fig. 2 shows the typical aspect of isotropic absorptions XAS and XMCD obtained for the three powders. Experimentally, isotropic spectra are obtained by recording the absorption of the sample with no applied field.

If the z -axis is chosen parallel to \mathbf{H} , the right-circular ϵ^- , the left-circular ϵ^+ and the linear ϵ^{\parallel} polarization vectors are defined as

$$\epsilon^- = \frac{1}{\sqrt{2}} \begin{pmatrix} 1 \\ -i \\ 0 \end{pmatrix}, \quad \epsilon^+ = -\frac{1}{\sqrt{2}} \begin{pmatrix} 1 \\ i \\ 0 \end{pmatrix},$$

$$\epsilon^{\parallel} = \begin{pmatrix} 0 \\ 0 \\ 1 \end{pmatrix}.$$

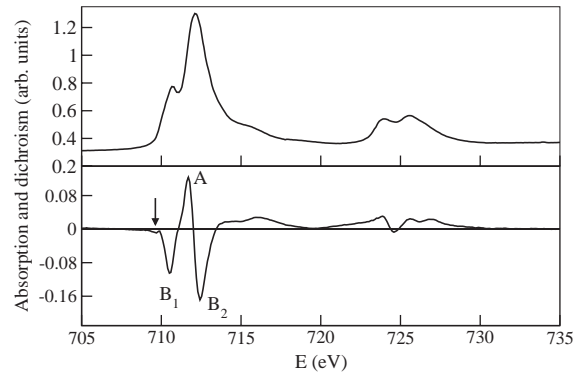


Fig. 2. Typical aspect of XAS and XMCD recorded on the samples.

In the electric dipole approximation, the three corresponding cross-sections are denoted as: $\sigma^- = \sigma^{\uparrow\downarrow} = \sigma^{\downarrow\uparrow}$, $\sigma^+ = \sigma^{\uparrow\uparrow} = \sigma^{\downarrow\downarrow}$, and σ^{\parallel} . The isotropic cross-section is given by $\sigma_{\text{iso}} = (\sigma^+ + \sigma^- + \sigma^{\parallel})/3$. We know from the HRTEM study that the crystallites are oriented at random with respect to the applied magnetic field. In this case, the magnetic linear dichroism is negligible, and $\sigma^{\parallel} \simeq (\sigma^+ + \sigma^-)/2$ [14]. Consequently, $\sigma_{\text{iso}} \simeq (\sigma^+ + \sigma^-)/2$, and the experimental quantity $(\sigma^{\uparrow\uparrow} + \sigma^{\downarrow\downarrow} + \sigma^{\uparrow\downarrow} + \sigma^{\downarrow\uparrow})/4$ is a good approximation of σ_{iso} . For each series of scans, this expression is used to normalize the isotropic absorption to unity at the maximum of the L₃ edge.

XMCD experimental signals are characteristic of the γ -Fe₂O₃ phase [22]. At the L₃ edge, they

consist of a positive peak (denoted A) and two negative peaks (denoted B1 and B2). At the $L_{2,3}$ edge signals are mostly positive. XMCD spectra at the $L_{2,3}$ edges are mainly determined by the strength of the spin–orbit coupling due to the initial $2p$ core–hole and by the spin polarization of the empty final localized $3d$ states [20]. The core–hole spin–orbit coupling splits the edges into the L_3 edge, resulting from the $2p_{3/2} \rightarrow 3d$ transition, and into the L_2 edge, resulting from the $2p_{1/2} \rightarrow 3d$ transition. XMCD allows to separate and to quantify the magnetic contributions of Fe_A^{3+} and Fe_B^{3+} ions to the magnetization. As shown by LFM calculations in Fig. 3, XMCD is reversed in sign between L_3 and L_2 edges for Fe_B^{3+} and Fe_A^{3+} ions. For atomic magnetic moments oriented parallel to the external magnetic field, the XMCD is negative at the L_3 edge and positive at the L_2 edge. This is the case of Fe_B^{3+} ions. The spins of Fe_A^{3+} ions are coupled antiferromagnetically with the spins of Fe_B^{3+} ions, as the main magnetic coupling is the antiferromagnetic coupling between A and B sites. Spins of Fe_A^{3+} ions are oriented in a direction opposite to

the external magnetic field. The sign of the dichroic contribution of the Fe_A^{3+} ions to XMCD is then opposite to the sign of the dichroic contribution of the Fe_B^{3+} ions. The Fe_A^{3+} contribution is positive at the L_3 edge and negative at the L_2 edge [23,22]. The XMCD signal of γ - Fe_2O_3 derives from the superposition of the contributions of Fe_A^{3+} and Fe_B^{3+} ions. The B1 and B2 peaks come from Fe_B^{3+} ions and the positive A peak from Fe_A^{3+} ions.

For Fe_A^{3+} and Fe_B^{3+} ions, one needs only the $10Dq$ parameter to describe the symmetry and the strength of the crystal field. Experimental data extracted from reflectance spectra of maghemite gives an octahedral crystal field of $10Dq = 1.9$ eV [24–26]. Concerning the tetrahedral sites, experimental values of $10Dq$ are available for Fe^{3+} ions as impurities in various matrices [27–29]. In our calculations, we use crystal field parameters close to but slightly smaller than those extracted from optical spectroscopy, due to $2p$ hole in the excited state. For Fe_B^{3+} ions, $10Dq = 1.5$ eV, and for Fe_A^{3+} ions, $10Dq = 0.7$ eV. The value of the octahedral crystal field is also consistent with the values found in literature for Fe^{3+} multiplet calculations on iron oxides [30–34]. For the $3d^5$ electronic configuration of Fe^{3+} ions the orbital part is fully symmetric (${}^6A_{1g}$ in O_h). Slight symmetry distortions around the ion would induce small modifications of XAS and XMCD signals. Such effects could not be detected on the recorded spectra. The above mentioned existence of distortions around Fe^{3+} ions with respect to perfect octahedral or tetrahedral symmetries in the case of MP phosphated particles is thus not detected from XMCD measurements. Values of octahedral and tetrahedral crystal fields are also dependent on the value of κ , that accounts for the covalency of the Fe–O bond. κ is defined by Racah parameters, $\kappa = B/B_0$, where B_0 is the Racah parameter for an isolated Fe^{3+} ion. Using Slater’s integrals, $B_0 = (1/49)F^2(3d, 3d) - (5/441)F^4(3d, 3d)$. For Fe^{3+} , we obtain $B_0 = 160$ meV. We used $\kappa = 55\%$, so the B Racah parameter for Fe^{3+} ions in the solid is of 88 meV. This value is close to the 72 meV value derived from reflectance spectra of γ - Fe_2O_3 [24]. For both the Fe_B^{3+} and the Fe_A^{3+} ions, ζ_{3d} is fixed to its atomic Hartree–Fock value of 74 meV. To

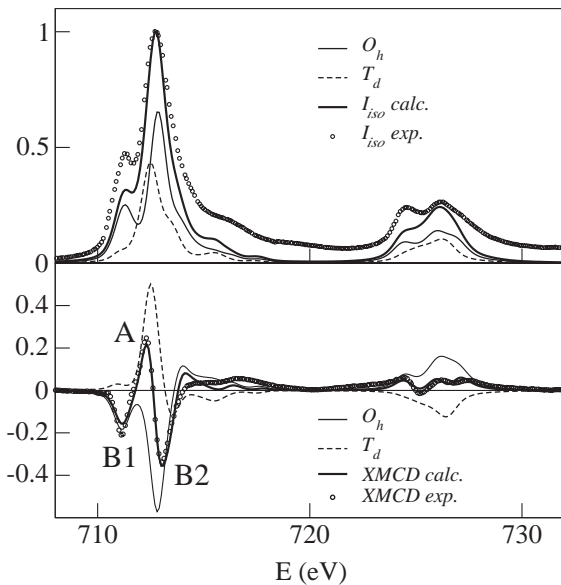


Fig. 3. Multiplet calculation of isotropic absorption and XMCD for Fe_A^{3+} and Fe_B^{3+} ions, along with the weighted averages for $A/B = 3/5$. Comparison to experimental isotropic spectrum and XMCD of 8 nm particles.

account for the experimental isotropic data, the value of ζ_{2p} is set to 8.4 eV. We performed calculations using an exchange-field parameter of 20 meV, at 4.2 K $\Gamma = 0.2$ eV for the Lorentzian broadening function at the L_3 edge, $\Gamma = 0.4$ eV at the L_2 edge and $\sigma = 0.25$ eV for the Gaussian instrumental broadening function [35,36,19].

Fig. 3 presents the calculated contributions of Fe_B^{3+} and Fe_A^{3+} ions to the isotropic absorption (upper panel) and to the XMCD signal (lower panel), and the experimental XAS and XMCD recorded on 8 nm particles at 2 T and 4.2 K. The isotropic cross-section of Fe_B^{3+} ions is much different from the isotropic cross-section of Fe_A^{3+} ions. From the quantitative analysis of Fe_B^{3+} and Fe_A^{3+} isotropic contributions, it is possible to determine roughly the A/B sites-ratio of the structure. Simulations of Fig. 3 are compatible with the bulk maghemite A/B = 3/5 sites ratio, with an absolute uncertainty of about 10%. The weighted sum of the isotropic cross-sections using this ratio is also represented. Nevertheless, from the comparison of the experimental isotropic cross-sections of the different samples, we estimate that the difference in the A/B sites ratio between S, M and MP particles is much smaller than the simulations uncertainty.

The intensity of the experimental dichroic signal of 8 nm particles measured between the maximum of the positive A peak and the minimum of the second negative B2 peak equals to 59% of the isotropic absorption at the maximum of the L_3 edge. We performed a simulation of XMCD considering an ideal ferrimagnetic alignment of the spins. The ratio of the magnetic contributions of Fe_B^{3+} and Fe_A^{3+} spins to XMCD (e.g. the absolute value of their projections in the direction of the applied field), denoted as m_A and m_B , is thus equal to the bulk A/B sites ratio: $m_A/m_B = 3/5$. A good agreement is obtained, except around 715 eV, where features are known to be due to configuration interactions. Consequently, the shoulder at 715 eV in the dichroic signal is overestimated by calculations. The B1 dichroic peak, as well as the corresponding low-energy first peak of the isotropic absorption at 711.3 eV are not exactly reproduced in width nor in intensity by our calculations. A possible explanation might be that

the corresponding group of transitions might have a core-hole broadening lower than $\Gamma = 0.2$ eV. Indeed, the intrinsic broadening mechanisms for each transition line are dependent on each final state reached [15,37]. Although such an effect has been observed at $M_{2,3}$ edges, it is usually considered negligible at $L_{2,3}$ edges [38]. A more convincing explanation would stem from charge transfer due to configuration interaction. At the L_2 edge, the low-energy isotropic peak at 724.5 eV is similarly too small compared to the main absorption peak. For $m_A/m_B = 3/5$, the calculated XMCD signal reproduces, nicely in shape and intensity, the other parts of the dichroic signal of the 8 nm particles. As discussed in the following, the magnetic order in 8 nm particles at 2 T and 4.2 K is close to that of bulk maghemite. As a consequence, the A/B sites occupation ratio and the m_A/m_B magnetic contributions ratio are identical.

The arrow in Fig. 2 indicates a small shoulder on the first negative peak of the dichroic signal at 710.3 eV. This shoulder is not observed on the dichroic spectra of other bulk spinels, such as NiFe_2O_4 , CoFe_2O_4 or $\text{Li}_{0.5}\text{Fe}_{2.5}\text{O}_{12}$ [23] and is not reproduced by the multiplet calculations either. It does not come from derivative effects and exists in all the recorded dichroic signals. This shoulder occurs at an energy matching with the chemical shift of Fe^{2+} ions. From multiplet calculations, we estimated this Fe^{2+} dichroic contribution to 4% of the total iron ions that we detect. As we measure XMCD in TEY, we are sensitive to the surface of grains that may undergo a reduction under UHV. Those traces may also be due to the synthesis method. These Fe^{2+} ions were not seen in Mössbauer because their concentration is below the detection limit.

3.3. XMCD of S particles vs. M particles

At the L_3 edge, the positive tetrahedral peak and the two negative octahedral peaks are, respectively, proportional to the projection of the magnetic moments of Fe_A^{3+} and Fe_B^{3+} ions along the external field. As a result, the intensity of the dichroic signal measured between A and B2 peaks is proportional to the magnetization of the sample,

as checked below. Magnetizations of the samples can be compared more precisely using the integrated absolute value of XMCD over L_3 and L_2 edges. This integral, denoted \mathcal{A} ($\mathcal{A} = \int_{L_2+L_3} |\sigma_{\text{XMCD}}| d(h\omega)$), is also proportional to macroscopic magnetization.

A comparison of the dichroic signals of the S, M and MP particles under a 2 T field at 4.2 K is reproduced in Fig. 4. Variations of the XMCD intensity of the different samples should be similar to the variations of the macroscopic magnetization measured by SQUID at the same field and temperature. The upper panel of the Fig. 4 shows the XMCD of the S and M samples. The peak-to-peak XMCD intensity of S particles is found to be equal only to 66% of the XMCD intensity of M particles. From XMCD intensity, the ratio of the magnetization of M particles to the magnetization of S particles is therefore $M_M/M_S \approx 1.5$ under 2 T and at 4.2 K. This lowering traduces the average greater misalignment of spins along the applied field in small particles. Consequently, a rescaled XMCD of S particles using a 1.5 multiplicative factor is also represented in Fig. 4, to compare the shapes of XMCD of M and S particles. The ratio of integrated absolute value of XMCD is close to the ratio of XMCD intensities: $\mathcal{A}_M/\mathcal{A}_S \approx 1.7$. At 2 T and 4.2 K, SQUID measurements give a

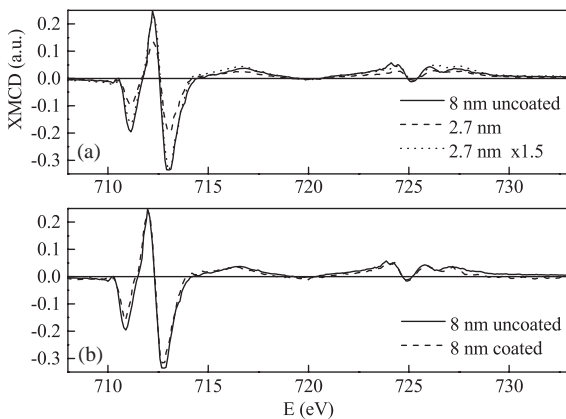


Fig. 4. XMCD of the S (2.7 nm), M (8 nm uncoated) and MP (8 nm phosphate-coated) nanoparticles recorded on SU23 (LURE) at 4.2 K under 2 T. (a): XMCD of S, M particles, and XMCD of S particles scaled by a 1.5 factor (b): XMCD of M and MP particles.

magnetization of $50 \text{ A m}^2 \text{ kg}^{-1}$ for the S particles [9] and $81 \text{ A m}^2 \text{ kg}^{-1}$ for the M particles (unpublished data). Magnetization of the S particles thus equals to 62% of the magnetization of the M particles, that is $M_M/M_S = 1.6$, in agreement with ratios of XMCD intensities and integrated absolute value of XMCD. At last, we noticed above that calculated XMCD considering the bulk structure of maghemite and experimental XMCD on 8 nm particles have close amplitudes. This agrees with the fact that 8 nm particles have a magnetization close to the bulk magnetization of $84 \text{ A m}^2 \text{ kg}^{-1}$.

XMCD spectra of 3 and 8 nm powders have similar shapes and are both consistent with $m_A/m_B = 0.6$. This result is confirmed by previous

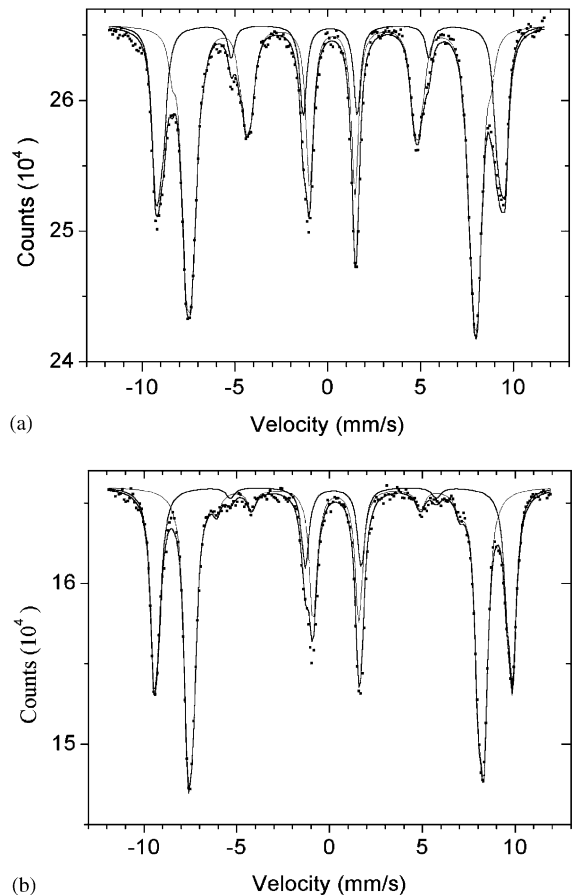


Fig. 5. In-field Mössbauer spectra of (a): 4.6 nm and (b): 8 nm particles (10 K, 6 T).

Table 1

Fraction of Fe^{3+} ions at A ($f_A(\%)$) and B ($f_B(\%)$) sites, A/B sites occupation ratio, average canting angles of Fe_A^{3+} ($\langle\theta\rangle_A$) and Fe_B^{3+} ($\langle\theta\rangle_B$) spins and the corresponding $(f \cos \theta)_A/(f \cos \theta)_B = m_A/m_B$ ratio for 4.6 and 8 nm powders of nanoparticles

Powder	f_A (%)	f_B (%)	A/B	$\langle\theta\rangle_A$	$\langle\theta\rangle_B$	$(f \cos \theta)_A/(f \cos \theta)_B$
4.6 nm	32 ± 0.5	68 ± 0.5	0.47	$27 \pm 2^\circ$	$48 \pm 2^\circ$	0.63
8 nm	37 ± 0.5	63 ± 0.5	0.59	$15 \pm 2^\circ$	$17 \pm 2^\circ$	0.60

in-field Mössbauer measurements on similar powders. Fig. 5 presents in-field Mössbauer spectra recorded at 10 K with a 6 T field parallel to the γ -ray on powders of 8 and 4.6 nm particles. The non-vanishing 2,5 lines of sextets are characteristic of spin canting [9]. Table 1 reports A/B sites ratio and $\langle\theta\rangle_A$, $\langle\theta\rangle_B$ canting angles of Fe_A^{3+} and Fe_B^{3+} spins deduced from Mössbauer spectra. From these data, we evaluate the ratio of projections of Fe_A^{3+} and Fe_B^{3+} spins in the direction of the applied field: $m_A/m_B = (f \cos \theta)_A/(f \cos \theta)_B$. This ratio is found equal to 0.60 for 8 nm particles and to 0.63 for smaller 4.6 nm particles. This trend is fully consistent with XMCD results, that give a constant $m_A/m_B = 0.6$ ratio going from M to smaller S particles. In-field Mössbauer measurements indicate a simultaneous increase of A/B and $\langle\theta\rangle_B/\langle\theta\rangle_A$ as the surface to volume ratio of particles increases, resulting in a constant value of m_A/m_B despite an increased spin disorder.

3.4. XMCD of M particles vs. MP particles

The lower panel of Fig. 4 compares the dichroic signals of the M and of the MP nanoparticles. At the L_3 edge, the corresponding isotropic spectra (not represented) are quite similar in shape and intensity, which allows a direct comparison between the dichroic signals. The XMCD intensity of phosphate-coated particles is 93% of the XMCD intensity of uncoated particles. In a similar way, the ratio of \mathcal{A} integrals for M and MP particles is of $\mathcal{A}_{MP}/\mathcal{A}_M \simeq 88\%$. This ratio is of the same order than the ratio of XMCD intensities. At 2 T and 4.2 K, SQUID measurements give magnetizations of 81 and 71 $\text{A m}^2 \text{kg}^{-1}$ for the M and MP powder samples [9]. The SQUID measurements are given with a 10% experimental uncertainty,

due to the H_2O content of the powders. Following these results, the magnetization of phosphate-coated particles equals to 88% of the magnetization of uncoated particles. Magnetization reductions estimated from XMCD and from SQUID are of similar magnitudes, on account of experimental uncertainties.

In-field Mössbauer spectra on the MP powder at 10 K show a strongly perturbed magnetic sub-pattern [9]. It stems from the freezing of a paramagnetic surface layer of Fe^{3+} ions caused by the phosphate ligands, in a totally magnetically disordered shell. The relative area of the perturbed magnetic sub-pattern and the magnetic sextet measured by Mössbauer show that 21% of the Fe atoms are bounded to phosphate groups and are magnetically disordered [9]. Comparison of XMCD of M and MP particles also points out this magnetic disorder. As shown in Fig. 4(b), the lowering of the dichroic intensity between M and MP particles comes from the reduction of the intensities of the two negative B1 and B2 octahedral peaks at the L_3 edge, without any modification of the intensity of the positive A tetrahedral peak that keeps the same intensity for M and MP samples. Intensities of the two octahedral peaks are reduced by 10% for MP particles with respect to M particles. Thanks to LFM calculations, the raise of the $A/|B2|$ intensity ratio resulting from this reduction can be linked quantitatively to the increase of the ratio of magnetic contributions of Fe_A^{3+} and Fe_B^{3+} ions, m_A/m_B . Fig. 6 displays results of multiplet calculations with the parameters used above, assuming a progressive reduction of the contribution of Fe_B^{3+} spins to the dichroic signal. The m_A/m_B magnetic contributions ratio ranges from the ideal bulk ratio ($m_A/m_B = 0.60$) to $m_A/m_B = 0.75$. The corresponding $A/|B2|$ intensity ratio

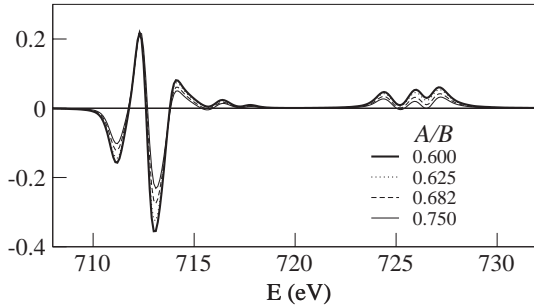


Fig. 6. Multiplet calculations of XMCD for several A/B site ratios in γ -Fe₂O₃.

ranges from 0.62 to 0.95. Variations of the m_A/m_B ratio does affect the shape of the dichroic peaks at the L₃ edge. But the ratio of the intensity of the second negative peak to the first negative peak remains unchanged. Magnetic contributions ratio variations only modify the relative intensity of the A tetrahedral peak to the B1 and B2 octahedral peaks. The 10% reduction of |B2| from M to MP particles is reproduced by calculations using $m_A/m_B \simeq 0.63$ instead of 0.60 in the absence of magnetic disorder. Differences in the intensities of the B1 and B2 peaks going from M to MP particles thus happen to be due to a reduction of the magnetic contribution of Fe_B³⁺ ions in phosphate-coated particles. In the case of a phosphate-modified surface, XMCD measurements indicate that the surface disordered spins could be mainly Fe_B³⁺ spins.

3.5. XMCD field dependence

Apart from the preceding case of a modified surface, the contrast between core and surface magnetic behaviors shall become perceptible under low magnetic fields, leading us to collect XMCD signals at low applied fields. Hysteresis loops presented in Ref. [10] for S and M powders show that the closure field of the loops is of 2 T for S particles and of 0.5 T for M particles, indicating a surface-related irreversibility. To follow the hysteresis loops during XMCD measurements, we rise the magnetic field up to a value of +2 T, before decreasing it to the required positive value for the measurement. We apply an equivalent procedure

for negative fields. Fig. 7 presents the dichroic signals of the S particles at the L₃ edge, varying the external field. On the left panel of the picture, spectra are plotted as-obtained, the isotropic absorption being normalized to 1 at the L₃ maximum. On the right panel of the picture, they are rescaled so as to get a same area for A peaks. Scaling factors are specified on the figure. To quantify XMCD signals, intensities of A, B1 and B2 dichroic peaks as a function of the applied field and A/|B2| intensity ratios are listed in Table 2. The corresponding m_A/m_B ratios deduced from LFM calculations are indicated. This table also give values of integrated absolute value of XMCD over L_{2,3} edges.

When the applied magnetic field decreases, the intensity of XMCD decreases as well, as indicated by decreasing values of \mathcal{A} , reflecting a loss of the average projection of the magnetic moments of the particles along the applied field. The rescaled spectra show that at 2 and 0.5 T, the relative intensities of the positive and the negative dichroic peaks are similar. However, for data collected at 0.4 and 0.2 T, the B1 and B2 peaks become clearly smaller compared to the A peak, as shown by the increase of A/|B2| when the applied field decreases. On the rescaled XMCD signals, the intensity of the B2 peak is reduced by about 30% compared to its intensity at higher fields. In the 2.7 nm particles, this observation evidences a

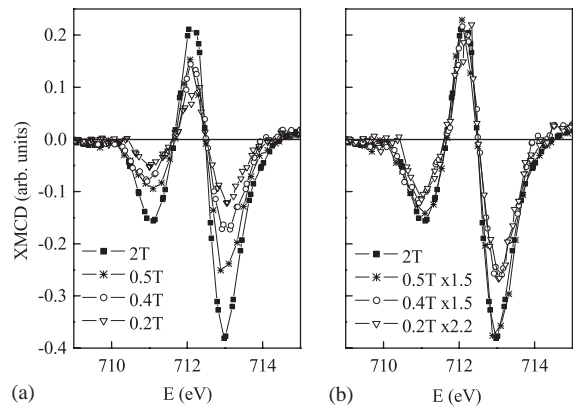


Fig. 7. (a): XMCD of the S (2.7 nm) nanoparticles at the L₃ edge recorded on BACH (Elettra) at 4.2 K under 0.2, 0.4, 0.5 and 2 T. (b): Rescaled XMCD spectra. The positive tetrahedral peaks all have the same area.

Table 2

Characteristics of XMCD spectra of S particles for different external fields: intensities of A, B1 and B2 dichroic peaks at $L_{2,3}$ edges, A/|B2| intensity ratios, simulated m_A/m_B ratios and integrated absolute value of XMCD

Field (T)	A	B1	B2	A/ B2	m_A/m_B	\mathcal{A}
2	0.21	-0.16	-0.38	0.55	0.57	1.00
0.5	0.15	-0.094	-0.25	0.61	0.60	0.64
0.4	0.14	-0.081	-0.17	0.83	0.69	0.54
0.2	0.10	-0.052	-0.12	0.83	0.69	0.38

preferential low-field spin disorder involving spins of octahedral Fe^{3+} ions. LFM results show that this reduction corresponds to $m_A/m_B = 0.69$ instead of 0.60 in the bulk material.

To check whether this canting has a surface origin, we performed the same measurements on the bigger M and MP particles. For M particles, the B1 and B2 octahedral peaks are reduced by 4% going down from 2 to 0.2 T, whereas, no reduction is observed for tetrahedral peaks. This reduction is weak (and lies in the uncertainty range) compared to the 30% reduction of the intensity of the B1 and B2 dichroic peaks in the case of S particles. As the relative reduction of the intensity of dichroic octahedral peaks with respect to the tetrahedral peak is connected to a growing magnetic disorder of spins of Fe_B^{3+} ions, the spins misalignment on octahedral sites happens to be weaker in M particles than in S particles, especially at low magnetic fields. As a matter of fact, M particles have a reduced surface to volume ratio, compared to S particles. In S particles, 50% of the Fe^{3+} ions are located at the surface (e.g. in a 0.35 nm thick layer), versus only 20% in M particles. Surface effects are therefore, expected to be weaker in M particles than in S particles, in agreement with the experimental result. A straight quantitative comparison between field-induced variations of XMCD in S and M particles must take into account the probing depth of 45 Å [11], larger than the 2.7 nm diameter of S particles and smaller than the 8 nm diameter of M particles. The surface relaxation of M particles might be even smaller than 4%, indicating an even more contrasted behavior than with S particles.

No relative field-induced variations of the contributions of the Fe_B^{3+} ions versus Fe_A^{3+} ions were observed for MP particles. As explained

above, at 4.2 K, surface spins of phosphate-coated particles are frozen in a disordered configuration. As a consequence, the magnitude of the external field has almost no effect on their magnetic order.

4. Conclusion

The examination of the isotropic cross-sections of 2.7 nm, 8 nm and phosphated 8 nm particles indicates that these three types of particles have similar A/B site occupation ratios. Thanks to XMCD signals recorded with decreasing values of the applied field, we detected at low fields on 2.7 and 8 nm particles a greater disorder of Fe_B^{3+} spins with respect to the field direction than for Fe_A^{3+} spins. Furthermore, this disorder is more important for the smaller 2.7 nm particles that have the largest surface to volume ratio. This observation agrees with the comparison of the magnetic contributions of Fe_B^{3+} and Fe_A^{3+} spins in 8 nm and phosphated 8 nm particles, the latter presenting a magnetically disordered surface, as shown previously by Mössbauer. Indeed, we also find a greater spin disorder of Fe_B^{3+} spins in phosphated 8 nm particles than in 8 nm particles, the magnetic contribution of Fe_A^{3+} spins remaining unchanged.

These two results jointly proves the existence of a preferential spin canting of Fe_B^{3+} spins at the surface. These results are consistent with the core-shell model of the magnetic structure formerly proposed for the particles. A possible explanation for this structure is that surface spins experience weakened exchange interactions with their neighbors, yielding to an increased disorder of Fe_B^{3+} spins at low-magnetic fields, typically below 500 mT for the small particles.

Acknowledgements

This work could not have been carried out without the very-low temperature cryostat developed by one of us in collaboration with J.-P. Kappler. We thank the staffs of the SU23 beamline (LURE) and of the BACH beamline (Elettra) for experimental help. We acknowledge J.-M. Grenèche (LPEC, University of Maine) for the recording of in-field Mössbauer spectra. We are grateful for the use of the Jeol 2010F TEM provided by the Centre Pluridisciplinaire de Microscopie et de Microanalyse (CP2M) at the University of Aix-Marseille III. This is IGP contribution number #2922.

References

- [1] J.L. Dormann, D. Fiorani, E. Tronc, *Magnetic Relaxation in Fine-particle Systems*, Advances in Chemical Physics, Wiley, New York, 1997.
- [2] J.-L. Dormann, D. Fiorani (Eds.), *Magnetic Properties of Fine Particles*, Delta Series, North-Holland, Amsterdam, 1992 (Application chapter).
- [3] R.H. Kodama, *J. Magn. Magn. Mater.* 200 (1999) 359–372.
- [4] H. Zijlstra, *Ferromagnetic Materials*, vol. 3, North-Holland, Amsterdam, 1982.
- [5] A.R.B. Castro, R.D. Zysler, M.V. Mansilla, C. Arciperete, M. Dimitrijewits, *J. Magn. Magn. Mater.* 231 (2001) 287–290.
- [6] J.M.D. Coey, *Phys. Rev. Lett.* 27 (1971) 1140–1142.
- [7] F.T. Parker, M.W. Foster, D.T. Margulies, A.E. Berkowitz, *Phys. Rev. B* 47 (1993) 7885–7891.
- [8] M.P. Morales, C.J. Serna, F. Bødker, S. Mørup, *J. Phys: Condens. Matter* 9 (1997) 5461–5467.
- [9] E. Tronc, A. Ezzir, R. Cherkaoui, C. Chanéac, H.K.M. Noguès, D. Fiorani, A.M. Testa, J.M. Grenèche, J.-P. Jolivet, *J. Magn. Magn. Mater.* 221 (2000) 63–79.
- [10] E. Tronc, D. Fiorani, M. Noguès, A. Testa, F. Lucari, F. D’Orazio, J. Grenèche, W. Wernsdorfer, N. Galvez, C. Chanéac, D. Mailly, J. Jolivet, *J. Magn. Magn. Mater.* 262 (2003) 6–14.
- [11] S. Gota, M. Gautier-Soyer, M. Sacchi, *Phys. Rev. B* 62 (2000) 4187–4190.
- [12] M. Zangrando, M. Finazzi, G. Paolucci, G. Comelli, B. Diviacco, R. Walker, D. Cocco, F. Parmigiani, *Rev. Sci. Instrum.* 72 (2001) 1313–1319.
- [13] P. Saintavit, J.-P. Kappler, *Magnetism and Synchrotron Radiation*, in: *Lecture Notes in Physics*, vol. 565, Springer, Berlin, 2001.
- [14] C. Brouder, J.-P. Kappler, *Magnetism and Synchrotron Radiation*, *Lecture Notes*, Les éditions de physique, 1997.
- [15] F.M.F. de Groot, J.C. Fuggle, B.T. Thole, G.A. Sawatzky, *Phys. Rev. B* 42 (1990) 5459–5467.
- [16] R.D. Cowan, *The theory of atomic structure and spectra*, Los Alamos series in basic and applied sciences, University of California Press, Berkeley, CA, 1981.
- [17] P.H. Butler, *Point Group Symmetry Applications: Methods and Tables*, Plenum Press, New York, 1981.
- [18] B.T. Thole, G. van der Laan, J.C. Fuggle, G. Sawatzky, R.C. Karnatak, J.-M. Esteva, *Phys. Rev. B* 32 (1985) 5107–5118.
- [19] M.-A. Arrio, P. Saintavit, C.C. dit Moulin, T. Mallah, M. Verdaguer, E. Pellegrin, C.T. Chen, *J. Am. Chem. Soc.* 118 (1996) 6422–6427.
- [20] G. van der Laan, B. Thole, *Phys. Rev. B* 43 (1991) 13401–13411.
- [21] P. Prené, PhD Thesis, Université Paris VI, France, 1996.
- [22] E. Pellegrin, M. Hagelstein, S. Doyle, H.O. Moser, J. Fuchs, D. Vollath, S. Schuppler, M.A. James, S. Saxena, L. Niesen, O. Rogojuan, G.A. Sawatzky, C. Ferrero, M. Borowski, O. Tjernberg, N.B. Brookes, *Phys. Stat. Sol. (B)* 215 (1999) 797–801.
- [23] F. Sette, C.T. Chen, Y. Ma, S. Modesti, N. Smith, *X-ray Absorption Fine Structure*, Ellis Horwood, Chichester, UK, 1991.
- [24] D.M. Sherman, T.D. Waite, *Am. Min.* 70 (1985) 1262–1269.
- [25] D.M. Sherman, *Phys. Chem. Miner.* 12 (1985) 161–175.
- [26] R.G. Burns, *Mineralogical Applications of Crystal Field Theory*, in: *Cambridge Topics in Mineral Physics and Chemistry*, vol. 5, Cambridge University Press, Cambridge, 1993, p. 224.
- [27] N.T. Melamed, F.de S. Barros, P.J. Viccaro, J.O. Artman, *Phys. Rev. B* 5 (1972) 3377–3387.
- [28] G.A. Waychunas, G.R. Rossman, *Phys. Chem. Miner.* 9 (1983) 212–215.
- [29] Z. Zheng-Wu, W. Ping-Feng, Y. Jian-Hua, Z. Kang-Wei, *Phys. Rev. B* 48 (1993) 16407–16409.
- [30] G. Cressey, C. Henderson, G. van der Laan, *Phys. Chem. Miner.* 20 (1993) 111–119.
- [31] G. van der Laan, I. Kirkman, *J. Phys: Condens. Matter* 4 (1992) 4189–4204.
- [32] P. Kuiper, B.G. Searle, P. Rudolf, L.H. Tjeng, C.T. Chen, *Phys. Rev. Lett.* 70 (1993) 1549–1552.
- [33] P. Kuiper, B. Searle, L.-C. Duda, R. Wolf, P. van der Zaag, *J. Electron. Spectrosc. Relat. Phenom.* 86 (1997) 107–113.
- [34] J. Crocombette, M. Pollak, F. Jollet, N. Thromat, M. Gautier-Soyer, *Phys. Rev. B* 52 (1995) 3143–3149.
- [35] J.C. Fuggle, J. Inglesfield (Eds.), *Unoccupied Electronic States*, *Topics in Applied Physics*, vol. 69, Springer, Berlin, 1992.
- [36] M.O. Krause, J.H. Olivier, *J. Phys. Chem. Ref. Data* 8 (1979) 329.
- [37] W.A. Caliebe, C.C. Kao, J.B. Hastings, M. Taguchi, A. Kotani, T. Uozumi, F.M.F. de Groot, *Phys. Rev. B* 58 (1998) 13452–13458.
- [38] K. Okada, A. Kotani, H. Ogasawara, Y. Seino, B.T. Thole, *Phys. Rev. B* 47 (1993) 6203–6206.